ROYAL SOCIETY
OF CHEMISTRY

PAPER

Check for updates

Sustainable nitrogen-doped carbon dots from biomass for ultrasensitive and selective fluorescent detection of isoliquiritigenin

Glowi Alasiri,[a] Ali M. Alaseem,[b] Ramadan Ali,[c] Al-Montaser Bellah H. Ali[d] and Mohamed M. El-Wekil 🆔 *[d]

Monitoring isoliquiritigenin (ISQ) is critical given its dual profile of therapeutic promise and dose-dependent toxicity, where precise quantification underpins safe administration, efficacy evaluation, and pharmaceutical quality control. In this study, we introduce a cost-effective and energy-efficient hydrothermal route for synthesizing nitrogen-doped carbon dots (NCDs) from potato peel biowaste, providing a sustainable pathway for agricultural waste valorization. The resulting NCDs exhibited bright green fluorescence with notable photostability and a quantum yield of 44.76%, enabling sensitive ISQ detection *via* a combined static-quenching and inner filter effect (IFE) mechanism, with a detection limit as low as 2.9 nM. The probe showed good selectivity in the presence of common interferents and satisfactory recovery values in spiked pharmaceutical and serum samples, meeting ICH M10 criteria for analytical performance. While these findings underscore the potential of biomass-derived NCDs as eco-friendly sensing platforms, key challenges must be addressed before clinical or point-of-care translation. These include comprehensive cytotoxicity evaluation, long-term colloidal stability in complex matrices, nanoparticle fate and clearance studies, and standardization of biomass inputs. Future studies should also explore scalable synthesis protocols, regulatory compliance pathways, and compatibility with miniaturized or wearable diagnostic devices. This work offers a promising step toward green nanotechnology for biomedical monitoring, while recognizing the critical hurdles that must be overcome for real-world implementation.

1. Introduction

Isoliquiritigenin (ISQ), a chalcone-type flavonoid predominantly isolated from the roots of *Glycyrrhiza uralensis*, has attracted considerable scientific interest due to its unique conjugated structure and multifunctional bioactivities. Beyond its traditional use in herbal medicine, ISQ exhibits pharmacological potential as an anticancer, anti-inflammatory, neuroprotective agent, and antioxidant, while also serving as a natural additive in food preservation and cosmetic formulations, highlighting its broad translational relevance.[1,2] In addition to its broad pharmacological profile, ISQ has emerged as a promising adjuvant in chemotherapy, where it mitigates drug-induced toxicity and enhances therapeutic efficacy. It also exerts potent anti-inflammatory effects in chronic disorders and

contributes to dermatological applications by accelerating wound healing, promoting tissue regeneration, and protecting against ultraviolet radiation-induced photoaging.[3,4] Despite its therapeutic promise, excessive intake of ISQ has been associated with adverse effects, underscoring the necessity for accurate and reliable quantification in biological and pharmaceutical samples.[5] Conventional analytical approaches such as capillary electrophoresis (CE)[6] and high-performance liquid chromatography (HPLC)[7] remain the standard tools for ISQ analysis; however, their routine application is limited by high operational costs, labor-intensive procedures, and long analysis times.[8] In contrast, fluorescence spectroscopy has emerged as a powerful alternative, offering superior sensitivity, high selectivity, rapid response, and user-friendly operation. Owing to these advantages, fluorescence-based methods are increasingly employed for monitoring bioactive compounds in clinical diagnostics, pharmaceutical formulations, and food safety assessments.[9–12]

Global pollution, driven by industrialization and unsustainable practices, increasingly threatens environmental and human health.[13] Around one-third of food is wasted annually, intensifying greenhouse gas emissions and economic losses.[14] Biomass waste is still mostly discarded or incinerated, causing resource loss and pollution.[15] This highlights the urgent need

[a] *Department of Biochemistry, College of Medicine, Imam Mohammad Ibn Saud Islamic University (IMSIU), Riyadh, 13317, Saudi Arabia*

[b] *Department of Pharmacology, College of Medicine, Imam Mohammad Ibn Saud Islamic University (IMSIU), Riyadh, Saudi Arabia*

[c] *Department of Pharmaceutical Chemistry, Faculty of Pharmacy, University of Tabuk, Tabuk 71491, Saudi Arabia*

[d] *Department of Pharmaceutical Analytical Chemistry, Faculty of Pharmacy, Assiut University, Assiut, 71526, Egypt. E-mail: mohamed.elwakeel@pharm.aun.edu.eg; mohamed.mohamoud@ymail.com*

for sustainable valorization to convert biomass into high-value materials for energy and industry—advancing both waste reduction and climate goals.

Biomass-derived carbon dots (CDs) have attracted increasing attention as sustainable nanomaterials; however, their structural and optical properties are often heterogeneous due to the intrinsic complexity of biomass precursors.[16] A diverse range of agricultural residues, food by-products, and industrial wastes have been exploited as carbon sources, offering both environmental and economic advantages in CD production.[17] Typically, biomass is composed of cellulose, hemicellulose, lignin, proteins, lipids, and inorganic ash, with the relative abundance of these constituents profoundly influencing the physicochemical features of the resulting CDs.[18] Among the available synthetic approaches, hydrothermal treatment and pyrolysis remain the most widely applied carbonization strategies, enabling scalable conversion of heterogeneous biomass into functional CDs with tunable fluorescence properties.[19] Emerging techniques, including microwave-assisted and enzymatic carbonization, are also being explored to enhance control over particle size, surface chemistry, and quantum yield, further broadening the application spectrum of biomass-derived CDs.

Heteroatom doping has emerged as a powerful strategy to modulate the physicochemical characteristics of carbon-based nanomaterials, significantly enhancing their electronic structure, surface chemistry, and optical performance.[20,21] By incorporating elements such as nitrogen, sulfur, phosphorus, or boron into the carbon framework, doped CDs exhibit improved charge transfer, tailored bandgap states, and enriched surface functionalities, thereby expanding their applicability in electrochemical energy storage, photocatalysis, bioimaging, and chemical/biological sensing.[22,23] Notably, a wide variety of heteroatom-doped CDs have been synthesized, many of which demonstrate remarkably strong and tunable photoluminescence, high quantum yield, and excitation-dependent emission, making them promising candidates for next-generation optoelectronic and biomedical platforms. For example, Tang *et al.* reported the synthesis of dual-emission CDs with fluorescence peaks at 520 and 668 nm using black pepper as a carbon source, which were successfully applied for the selective detection of Fe^{3+} ions. Interestingly, the fluorescence was recovered upon the addition of ascorbic acid due to its strong reducing capability, thereby demonstrating the feasibility of these CDs as a ratiometric probe for ascorbic acid sensing.[24] In a related study, Xue *et al.* fabricated dual-emission CDs from *Viburnum awabuki* leaves, further highlighting the versatility of biomass precursors in tailoring optical properties and enabling multifunctional sensing applications.[25]

In this study, biomass-derived nitrogen-doped carbon dots (NCDs) were synthesized through a facile hydrothermal process using potato peels. The resulting NCDs displayed strong and stable fluorescence emission, underscoring their suitability for
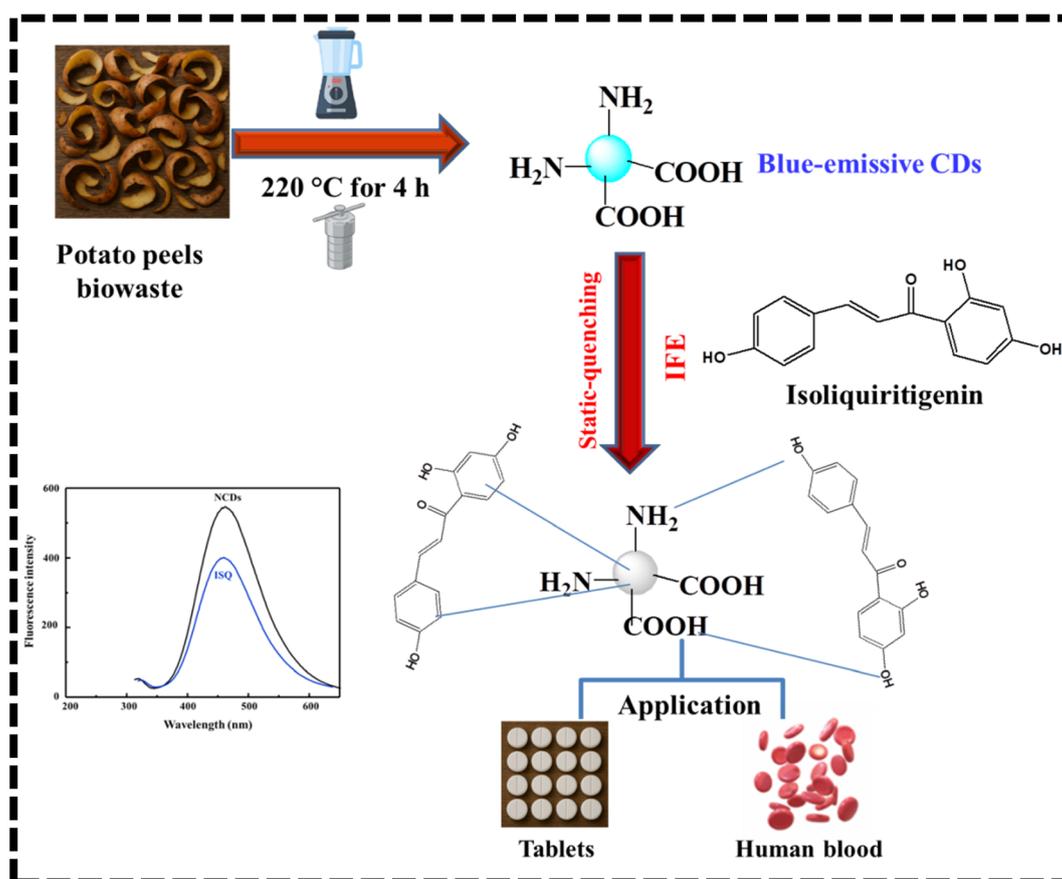
Scheme 1 Preparation of biowaste-based fluorescent NCDs for detection of ISQ.

sensing applications. Upon the introduction of ISQ, the fluorescence intensity of the NCDs was markedly quenched, a phenomenon attributed to a combination of static quenching and the inner filter effect (Scheme 1). Leveraging this mechanism, a sensitive and reliable fluorescent sensing platform was established for ISQ detection. The method demonstrated high analytical performance, achieving accurate quantification in tablets and plasma samples with satisfactory recovery values and low relative standard deviations (RSDs), thereby confirming its reproducibility and practical applicability.

2. Experimental

2.1. Materials and reagents

Isoliquiritigenin (ISQ, 98.8%), uric acid (98.3%), dopamine (99.5%), glucose (98.8%), glutathione (98.4%), glycine (98.8%), cholesterol (97.9%), cysteine (97.7%), lysine (97.4%), alanine (99.9%), phenylalanine (98.7%), histidine (98.8%), glutamic acid (97.8%), tryptophan (98.9%), ascorbic acid (98.6%), and quinine sulfate (98.8%) were obtained from Sigma–Aldrich (USA). Inorganic salts, including K_2HPO_4, KH_2PO_4, HCl, NaOH, NaCl, KCl, Na_2SO_4, $CaCl_2$, $BaCl_2$, and $ZnCl_2$, were purchased from Merck (Germany). Ultrapure water (resistivity 18.2 MΩ cm, Milli-Q system) was used throughout all experimental procedures.

2.2. Instruments

The optical properties of NCDs were systematically analyzed using a Shimadzu UV-Vis spectrophotometer (Model 1601 PC, 200–800 nm range) and a Shimadzu RF-5301 PC fluorescence spectrometer. Synthesis was performed using an AICIL muffle furnace, followed by uniform dispersion achieved through magnetic stirring with an IKA C-MAG HS7 hotplate stirrer. Functional groups present on the surface were identified *via* Fourier-transform infrared spectroscopy (FTIR, Nicolet™ iSTM10, 4000–400 cm^{-1}). Transmission electron microscopy (TEM, JEOL JEM-100CX II) was employed to investigate the morphology and internal lattice structures. The crystalline phases and structural organization were characterized through X-ray diffraction (XRD) using a Panalytical X'Pert Pro system with Cu Kα radiation, scanned from 5° to 90° at a rate of 2° min^{-1}. To evaluate photoluminescence robustness under varying conditions, fluorescence stability at different pH levels was monitored using a Mettler Toledo digital pH meter. Absolute quantum yield measurements were conducted using quinine sulfate (54% in 0.1 M H_2SO_4, excitation at 310 nm) as a calibration standard. In addition, the surface elemental distribution and chemical state composition were examined using X-ray photoelectron spectroscopy (XPS, Thermo Scientific EscalAB 250Xi), offering in-depth insight into the doping configuration and electronic structure of the synthesized NCDs. Dynamic light scattering (DLS) measurements were carried out using a Zetasizer Nano ZS (Malvern Instruments) to determine the particle size and size distribution of the samples.

2.3. Synthesis of NCDs

NCDs were synthesized through a sustainable hydrothermal approach using potato peels as a green carbon precursor. Potato peels were first oven-dried at 25 °C to remove residual moisture, finely ground into powder, and homogenized. A mixture of potato peel powder (5 g) and ultrapure water (30 mL) was magnetically stirred at 25 °C for 30 min to ensure uniform dispersion of the reactants. The prepared solution was placed into a 50 mL Teflon-lined stainless-steel autoclave and subjected to thermal treatment at 220 °C for 4 hours. Following natural cooling to room temperature, the resultant suspension was filtered through a 0.22 μm microporous membrane to remove coarse impurities, and subsequently centrifuged at 10 000 rpm for 15 minutes to further eliminate residual biomass. The clarified supernatant was then purified by dialysis using a 1000 Da molecular weight cut-off membrane against ultrapure water for 24 hours. Finally, the purified NCDs were obtained as a dry powder *via* freeze-drying, ensuring long-term stability and ease of re-dispersion for subsequent optical and sensing studies.

2.4. Detection steps

In preparation for fluorescence sensing, 300 μL of NCDs solution (2 mg mL^{-1}) was mixed with 700 μL of phosphate buffer (0.1 M, pH 7.0) to preserve both ionic strength and chemical stability. To this mixture, 500 μL of ISQ standard solutions with varying concentrations were added. The resulting solutions were gently mixed and incubated for 1.5 minutes to ensure sufficient interaction between the NCDs and the ISQ analyte. Fluorescence emission spectra were obtained using a 360 nm excitation wavelength, with emission intensity monitored at 440 nm, corresponding to the typical luminescence of the NCDs.

2.5. Preparation of samples

Twenty tablets of liquorice tablets (25 mg) were finely powdered and accurately weighed. Weight equivalent to amount of one tablet was extracted with 15 mL methanol *via* ultrasonic treatment for 15 minutes, followed by filtration. The extraction was repeated three times, and the combined filtrates were diluted to 50 mL with methanol.

Following centrifugation of plasma samples at 10 000 rpm for 5 minutes to eliminate cellular material, 1.5 mL of acetonitrile was introduced to the supernatant to precipitate endogenous proteins and mitigate matrix-related interferences. The solution was vortex-mixed and centrifuged again under the same parameters. The clarified supernatant was then collected and evaporated to dryness using reduced pressure. The remaining residue was reconstituted in ultrapure water and diluted 1 : 20 using 0.1 M phosphate buffer at pH 7.0 to mimic physiological conditions and ensure optimal fluorescence compatibility. Samples were analyzed immediately to preserve analyte stability.

2.6. Ethical approval and consent to participate

All experimental protocols involving human biological samples (serum and urine) were approved by the Institutional Ethical Committee Assiut University Clinics. Informed consent was obtained from all healthy adult volunteers prior to sample collection, in accordance with the Declaration of Helsinki.

3. Results and discussions

3.1. Characterization

TEM analysis demonstrated that the synthesized NCDs were predominantly spherical and well-dispersed without noticeable aggregation. As illustrated in Fig. 1A, the particle sizes ranged from 2.78 to 7.45 nm, with an average diameter of approximately 5.78 nm, confirming a narrow distribution and structural homogeneity (Fig. 1B). The inset high-resolution TEM (HRTEM) image further revealed distinct lattice fringes with an interlayer spacing of ∼0.224 nm, which can be attributed to the (002) crystallographic plane of graphitic carbon domains. This spacing is consistent with previously reported graphitic carbon structures and highlights the partial graphitization of the carbon core. Such well-resolved lattice fringes not only verify the crystalline nature of the NCDs but also suggest that sp^2-

hybridized carbon frameworks contribute to their strong optical and electronic properties, which are essential for fluorescence-based sensing applications.[26]

Raman spectroscopy provided further insight into the structural characteristics of the NCDs. As shown in Fig. 1C, two prominent bands were observed: the D band at ∼1353 cm^{-1}, corresponding to disordered carbon and sp^3-hybridized defects, and the G band at ∼1578 cm^{-1}, arising from the in-plane vibrations of sp^2-bonded carbon atoms within graphitic domains.[27] The calculated intensity ratio (I_D/I_G) was 1.28, indicative of a relatively high degree of disorder and abundant surface defects. Such structural disorder is advantageous, as defect states can act as radiative recombination centers, thereby enhancing the photoluminescence of the NCDs.[28] At the same time, the persistence of sp^2 domains ensures the retention of essential electronic conjugation, which is critical for
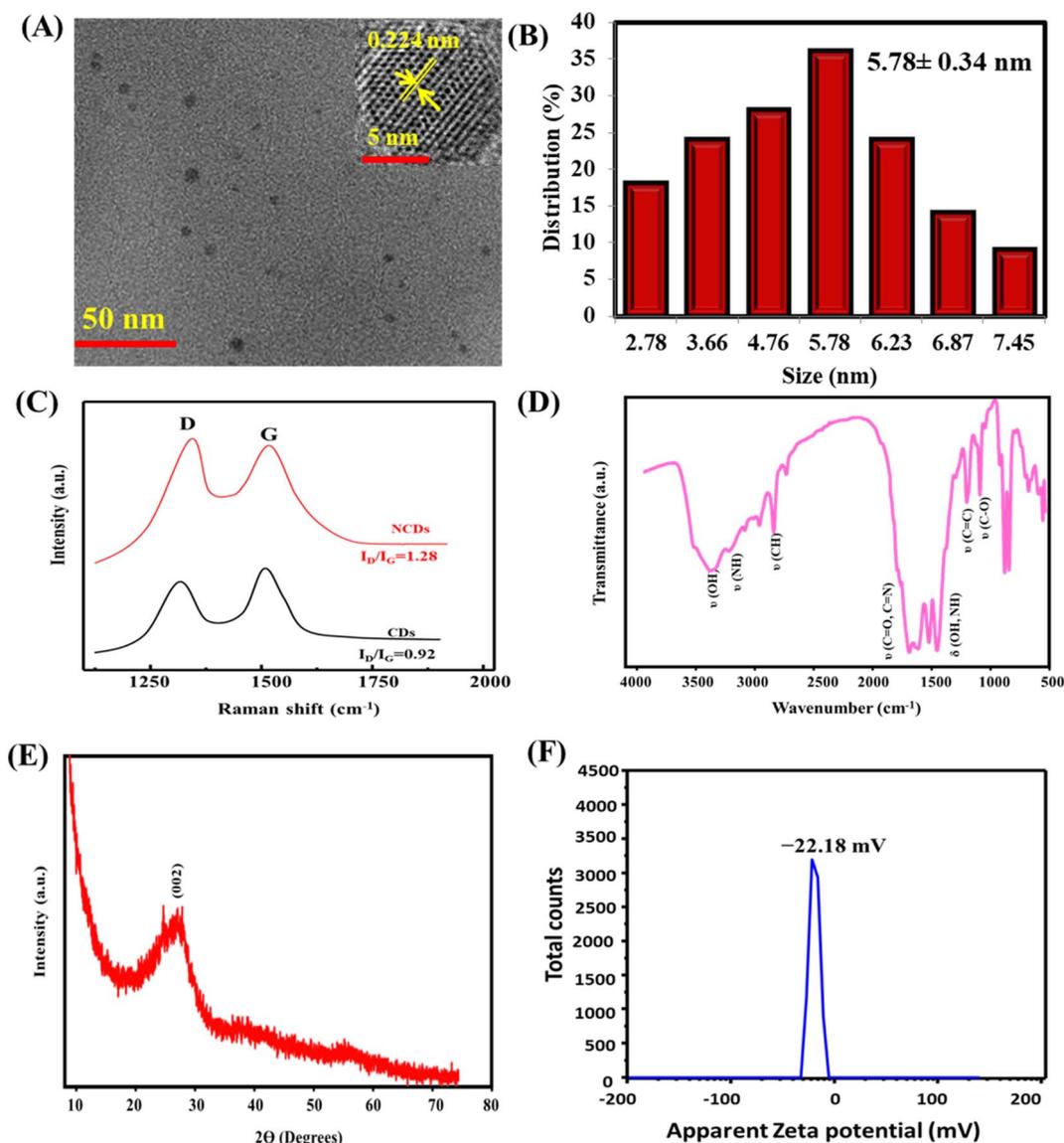

Fig. 1 SEM (A), size distribution (B), Raman spectra (C), FTIR (D), XRD (E), and zeta potential (F) of biowaste-derived NCDs. Raman spectrum of CDs is provided in (C) for comparison. The zeta potential was carried out in ultrapure water.

maintaining strong optical absorption and emission features.[29] This dual contribution of disordered and ordered domains suggests that the synthesized NCDs possess an optimized balance between defect-mediated emissive centers and graphitic frameworks, rendering them highly suitable for advanced applications in fluorescence sensing, bioimaging, and optoelectronic devices.

FTIR analysis revealed a range of surface functional groups, supporting successful surface passivation and heteroatom incorporation (Fig. 1D). The broad absorption bands at 3444 and 3278 cm^{-1} is assigned to O–H and N–H stretching, indicating presence of OH/NH groups, respectively. Aliphatic C–H stretching is evident at 2807 and 2865 cm^{-1}, suggesting the presence of alkyl chains. The sharp band at 1692 cm^{-1} reflects C=O/C=N stretching from carbonyl and amide groups, while peaks at 1476, 1330, and 1170 cm^{-1} correspond to C=C, O–H/N–H, and C–O stretching vibrations, respectively.[30,31]

XRD analysis further confirmed the structural features of the synthesized NCDs. As shown in Fig. 1E, a broad diffraction peak centered at approximately 23.34° was observed, which corresponds to the (002) reflection of graphitic carbon. The broadness of this peak suggests a low degree of long-range order and limited crystallinity within the sp^2 carbon domains, in line with the highly amorphous nature typically reported for biomass-derived carbon nanomaterials.[32,33] This disordered arrangement is consistent with the lattice fringes observed in the HRTEM images, supporting the coexistence of small graphitic domains embedded within a largely amorphous carbon matrix. Such structural features are advantageous, as the presence of short-range sp^2 clusters and abundant disordered regions often enhances surface reactivity and introduces defect states, which in turn promote the strong photoluminescence and versatile chemical functionality of NCDs. Collectively, the XRD and TEM findings validate that the synthesized NCDs possess a partially graphitized, defect-rich architecture favorable for sensing and bioimaging applications.

Zeta potential measurements revealed that the NCDs possessed a surface charge of −22.18 mV, reflecting the abundance of negatively charged functional groups such as carboxyl (–COOH) and hydroxyl (–OH) moieties on their surface.[34,35] This moderately high negative potential is advantageous, as it promotes electrostatic repulsion among particles, thereby minimizing aggregation and ensuring long-term colloidal stability in aqueous dispersions (Fig. 1F). Such stability is particularly important for biological and environmental applications, where consistent particle dispersion directly influences
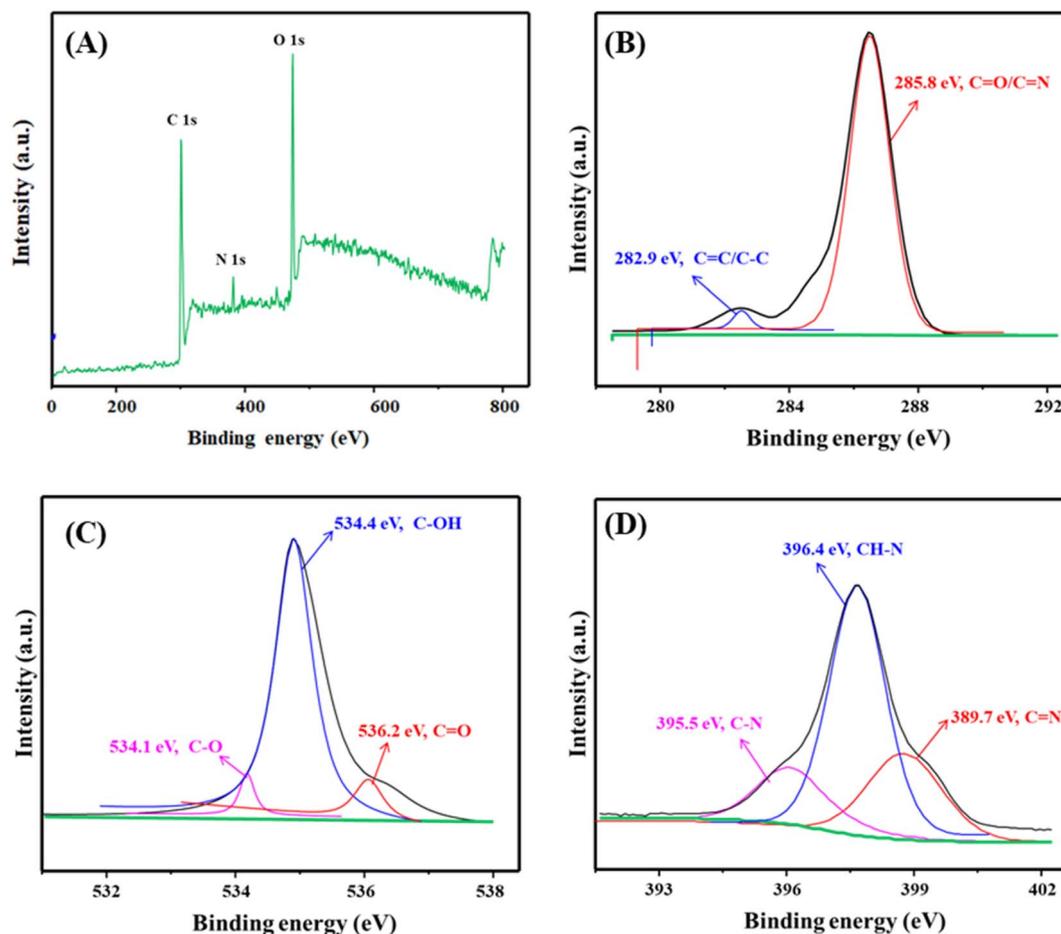

Fig. 2 (A) Full XPS survey of biowaste-derived NCDs; (B–D) deconvoluted spectra of C 1s, O1s, and N 1s, respectively.

reproducibility and reliability of performance. Moreover, the presence of oxygen-containing groups not only governs colloidal behavior but also enhances hydrophilicity and provides active sites for further functionalization or interaction with target analytes. These combined attributes render the synthesized CDs highly suitable for use in fluorescence sensing, bioimaging, and related aqueous-phase applications.

XPS provided detailed insights into the elemental composition and surface chemistry of the NCDs. The survey spectrum (Fig. 2A) displayed distinct C 1s, N 1s, and O 1s signals, confirming the incorporation of nitrogen and oxygen heteroatoms into the carbon framework. Deconvolution of the C 1s spectrum (Fig. 2B) revealed major contributions at 282.9 eV, assigned to sp^2-hybridized C=C/C–C bonds, and at 285.8 eV, corresponding to C=O and C=N functionalities, which indicate the coexistence of aromatic domains and heteroatom doping. The O 1s spectrum (Fig. 2C) displayed peaks at 534.1, 534.4, and 536.2 eV, attributable to C–O, C–OH, and C=O groups, respectively, suggesting the presence of abundant oxygenated species on the CD surface. Similarly, the N 1s spectrum (Fig. 2D) showed peaks at 395.5, 396.4, and 389.7 eV, corresponding to C–N, CH–N, and graphitic C=N species, confirming successful nitrogen incorporation into the lattice.[34] The coexistence of oxygen- and nitrogen-containing functionalities imparts dual advantages: (i) enhanced hydrophilicity and colloidal stability due to electrostatic repulsion and hydrogen bonding, and (ii) improved electron-donating and electron-withdrawing capacity, which can modulate the electronic states of the CDs and promote defect-mediated photoluminescence. These features highlight the significance of heteroatom doping in tailoring the optical properties and expanding the applicability of NCDs in sensing, bioimaging, and catalytic systems.

The UV-Vis absorption spectrum of the synthesized nitrogen-doped carbon dots (NCDs) displayed two distinct bands at 252 and 344 nm (Fig. 3A), corresponding to π–π^* transitions of aromatic C=C domains and n–π^* transitions associated with heteroatom-containing groups (*e.g.*, C=O, C=N). Unlike conventional molecular fluorophores with well-defined conjugated frameworks, the absorption profile of NCDs arises from the heterogeneous interplay of sp^2-hybridized carbon clusters, surface defect states, and heteroatom dopants, which collectively govern their unique photophysical behavior. Upon excitation at 375 nm, the NCDs exhibited a pronounced and stable blue emission centered at 465 nm, with negligible excitation dependence across the 345–395 nm range (Fig. 3B). The absolute photoluminescence quantum yield was determined to be 44.76%, a value that surpasses many biomass-derived carbon dots reported in recent literature, such as those synthesized from black pepper (10.25%),[24] Rambutan seed waste (16.87%),[28] and chicken feet (42.90%),[31] thereby highlighting the efficiency of the proposed synthetic strategy. This high quantum yield, coupled with excitation-independent emission, underscores the suitability of the NCDs for diverse technological applications, including bioimaging, fluorescence sensing, and energy-efficient optoelectronic devices such as light-emitting diodes. Moreover, the excitation-independent emission behavior suggests the presence of uniform emissive states, which is
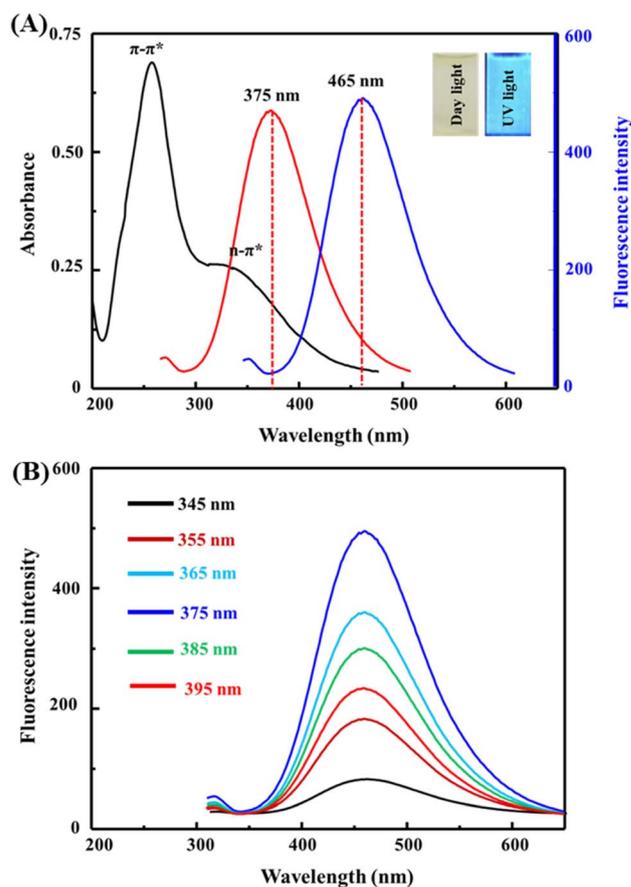

Fig. 3 (A) Absorption and photoluminescence spectra of biowaste-derived NCDs while (B) is variation of emission fluorescence with excitation wavelengths variation.

highly desirable for reproducible performance in analytical and biomedical applications.

The as-synthesized NCDs demonstrated remarkable stability under a wide range of physicochemical conditions. Their fluorescence intensity remained essentially unchanged at elevated temperatures up to 90 °C, confirming excellent thermal robustness (Fig. S1A). Likewise, prolonged UV irradiation for 180 min induced no significant loss of emission intensity, indicating strong resistance to photobleaching (Fig. S1B). The fluorescence signal was also largely insensitive to pH fluctuations across the tested range, highlighting the persistence of surface passivation and stable emissive states (Fig. S1C). Even in the presence of high ionic strength, with NaCl concentrations up to 3.0 M, only minor quenching was observed at the highest salt levels, confirming good colloidal stability against electrolyte-induced aggregation (Fig. S1D). Importantly, no evidence of fluorescence decay, spectral shift, or aggregation was detected after 83 days of storage under ambient conditions, underscoring their long-term durability (Fig. S1E). Collectively, these results demonstrate the superior environmental tolerance of NCDs compared to many reported carbon-based nanomaterials. Such robustness is crucial for their deployment in real-world applications, particularly in bioimaging, fluorescence sensing in complex matrices, and optoelectronic devices,

where stability under thermal, photonic, and ionic stress is essential.

3.2. Detection mechanism

Spectroscopic analyses confirmed that the NCDs possess abundant surface functionalities, including hydroxyl, carbonyl, carboxyl, and amino groups, which are well-known to facilitate interactions with target analytes. To elucidate the sensing mechanism, a combination of fluorescence emission, UV-Vis absorption, and time-resolved photoluminescence measurements was employed. These complementary techniques enabled evaluation of possible quenching pathways such as Förster resonance energy transfer (FRET), the inner filter effect (IFE), and static/dynamic quenching processes.[35] As shown in Fig. S2A, the absorption spectrum of ISQ exhibits a pronounced spectral overlap with the excitation band of the NCDs, suggesting the strong likelihood of FRET or IFE as major contributors to the observed fluorescence attenuation.[36,37]

In general, FRET is characterized by a marked decrease in fluorescence lifetimes, whereas the IFE has little to no impact on this parameter.[38] Additional insight was gained from UV-Vis absorption measurements, which showed a distinct red shift in the NCD–ISQ mixture (Fig. S2B). Such spectral shifts are indicative of ground-state complex formation, further supporting the role of static quenching.[39] Time-resolved photoluminescence studies revealed that the mean lifetime of NCDs decreased only slightly from 5.56 ns to 5.44 ns upon the addition of ISQ (Fig. S2C). This negligible variation suggests that IFE is the dominant pathway, although the contribution of static quenching cannot be excluded[40,41] To quantitatively probe the quenching mechanism, the Stern–Volmer (SV) relationship ($F_0/F = K_{SV}[Q]$) was applied. The calculated K_{SV} values at 298, 308, and 318 K were 1.53×10^6, 0.97×10^6, and 0.84×10^6 M^{-1}, respectively. The quenching constant (K_{SV}) was found to decrease with increasing temperature (Fig. S2D), consistent with a static quenching process where complex stability weakens at elevated temperatures.[42] The quenching of NCDs is attributed to static-quenching and IFE.

Our results collectively support a dual quenching mechanism dominated by static complex formation and IFE. Nevertheless, additional pathways commonly reported for carbon-dot-based probes merit consideration to strengthen the mechanistic interpretation. One possibility is the emergence of non-emissive ground-state aggregates formed through surface adsorption of ISQ.[43] Dynamic Light Scattering (DLS) analysis would provide a decisive evaluation of this scenario; a measurable increase in the hydrodynamic diameter following ISQ addition would be characteristic of aggregation-induced fluorescence suppression. In our system, however, such behavior appears improbable. The NCDs exhibit strong colloidal stability, reflected by their negative surface charge (-22.18 mV), resistance to ionic-strength perturbation, and the absence of morphological changes in TEM images even after exposure to 50 μM ISQ (Fig. S3A). These observations collectively argue against aggregation-driven quenching. Moreover, the minimal alteration in fluorescence lifetime reinforces the conclusion

that dynamic quenching processes—particularly photoinduced electron transfer (PET)—are not the primary contributors to signal loss.[44] The NCDs exhibited a zeta potential of -22.18 mV, and this value remained essentially unchanged upon the addition of ISQ. The absence of any appreciable shift in surface charge indicates that ISQ does not significantly perturb the NCD surface, supporting the conclusion that electrostatic attraction or surface adsorption is not a major contributor to the quenching mechanism. The two main quenching mechanisms are dynamic and static, which can be distinguished by temperature-dependent studies, fluorescence lifetime measurements, or shifts in UV-Vis absorption spectra.[45] In static quenching, a stable, non-fluorescent complex forms in the ground state, with reduced stability—and thus quenching efficiency—at higher temperatures. Dynamic quenching involves collisional interactions between excited fluorophores and quenchers, which increase with temperature due to enhanced diffusion.[46] A straight line emerges in the SV plot when the quenching process is 100% static or 100% dynamic,[47,48] Fig. S2D. Time-resolved fluorescence decay measurements were performed to elucidate the quenching pathway of the NCDs in the presence of increasing ISQ concentrations (Fig. S3B). Notably, the fluorescence lifetimes remained essentially unchanged upon ISQ addition, indicating that the emissive excited state of the NCDs is not significantly perturbed by the quencher. Such lifetime invariance is characteristic of a static quenching process, in which non-fluorescent ground-state complexes predominate and the decay kinetics of the uncomplexed fluorophore remain unaltered. These findings, together with the Stern–Volmer behavior and spectral analyses, further corroborate the predominance of a static-quenching mechanism rather than dynamic collisional quenching.[49]

3.3. Conditions optimization

The synthetic parameters for producing NCDs from biowaste were systematically optimized by evaluating the influence of reaction temperature and time, with fluorescence intensity selected as the primary performance indicator (Fig. S4). The strongest emission was achieved under hydrothermal conditions of 220 °C for 4 h, highlighting the critical role of both thermal energy and reaction duration in promoting the formation of stable emissive centers. These optimized conditions are likely to accelerate the carbonization process and enhance surface passivation, thereby generating abundant functional groups that stabilize radiative recombination sites. Similar trends have been observed in previous reports, where extended thermal treatment at appropriate temperatures facilitated the development of graphitic domains and nitrogen-related defects, both of which are essential for efficient fluorescence emission. In addition, the balance between excessive carbonization (which can diminish quantum yield due to aggregation and non-radiative pathways) and insufficient passivation (which leaves surface traps unsaturated) underscores the necessity of precise control over reaction parameters. Thus, the optimized protocol not only maximizes photoluminescence but also provides insights into the mechanistic

interplay between structural ordering, defect incorporation, and surface state engineering during NCD formation.[50,51]

To achieve the highest sensitivity and reliability in detecting ISQ, the critical sensing parameters of biowaste-derived NCDs were systematically optimized (Fig. S5). The influence of NCD concentration (0.5–3.5 mg mL^{-1}), solution pH (5–9), and incubation time (0.5–5 min) was carefully evaluated. As shown in Fig. S5A, fluorescence quenching efficiency increased progressively with rising NCD concentration, reaching a maximum at 2.0 mg mL^{-1}, beyond which signal enhancement plateaued due to inner filter effects and potential aggregation. The effect of pH was particularly significant, with the optimal response observed at physiological pH (7.0) (Fig. S5B). At this condition, deprotonated carboxyl and hydroxyl groups on the NCD surface enhanced attraction with ISQ *via* hydrogen bonding and π–π stacking interactions stabilized the probe–analyte complex. Kinetic investigations revealed that fluorescence quenching occurred rapidly, with equilibrium binding established within 1.5 min, underscoring the probe's fast response and operational practicality (Fig. S5C). Collectively, the optimized sensing conditions were determined as 2.0 mg mL^{-1} NCDs, pH 7.0, and 1.5 min incubation, which balance probe stability, interaction strength, and rapid detection capability.

To evaluate reproducibility and scalability, five independent batches of NCDs were synthesized under identical hydrothermal conditions. As shown in Table S1 and Fig. S6, the quantum yield exhibited minimal batch-to-batch variation (RSD = 0.49%), and the emission maxima remained stable at ~465 nm across all preparations. The average yield was 22.1 ± 0.27 mg per 5 g of biomass input, corresponding to ~0.44% w/w. Purity of each batch was confirmed *via* UV-Vis and dialysis (1000 Da cut-off), with negligible baseline drift and consistent removal of small-molecule impurities. Zeta potential measurements (−22.1 to −22.5 mV) confirmed colloidal stability. These findings underscore the method's reproducibility and potential for scaled-up preparation with minimal performance deviation.

3.4. Detection of ISQ

The analytical sensitivity of the biowaste-derived NCD probe toward ISQ was systematically evaluated across a broad concentration range. As illustrated in Fig. 4A, a progressive decrease in fluorescence intensity was observed with increasing ISQ levels, confirming efficient quenching of the NCD emission. The quantitative response exhibited an excellent linear correlation between (F_0/F) and ISQ concentration from 0 to 500 μM, following the regression equation (F_0/F) = 0.006[ISQ] + 1.1217 with a high correlation coefficient (R^2 = 0.9982) (Fig. 4B). Based on the $3\sigma/k$ criterion, where σ represents the standard deviation of ten replicate blank measurements and k is the calibration slope, the limit of detection (LOD) was determined to be 0.0029 μM, demonstrating remarkable sensitivity. When benchmarked against conventional fluorescence probes and chromatographic or electrochemical techniques (Table 1), the present NCD-based platform shows multiple advantages: simplified preparation, rapid detection within minutes, high sensitivity, an extended linear working range, and an ultralow LOD. Furthermore, the green synthesis route from renewable biowaste enhances its sustainability credentials, addressing both analytical performance and environmental impact. These attributes collectively position the NCD probe as a cost-effective and eco-friendly alternative for trace detection of ISQ, with potential applicability in biomedical and food analysis.

While the NCD synthesis is environmentally favorable due to its aqueous, solvent-free nature and utilization of food waste, a quantitative assessment of its environmental footprint relative to conventional platforms reveals additional advantages. The total energy input per batch (~1.0 kWh) is significantly lower than that of chromatographic methods (1.8–2.5 kWh per run), and no hazardous solvents or reagents are required, minimizing chemical waste and regulatory burdens. Furthermore, no heavy metals or persistent pollutants are involved, reducing concerns over nanoparticle leaching (Table S2). However, potential caveats for large-scale application include limited batch volumes due to autoclave capacity, batch-to-batch variability in biowaste composition, and the need for standardized raw
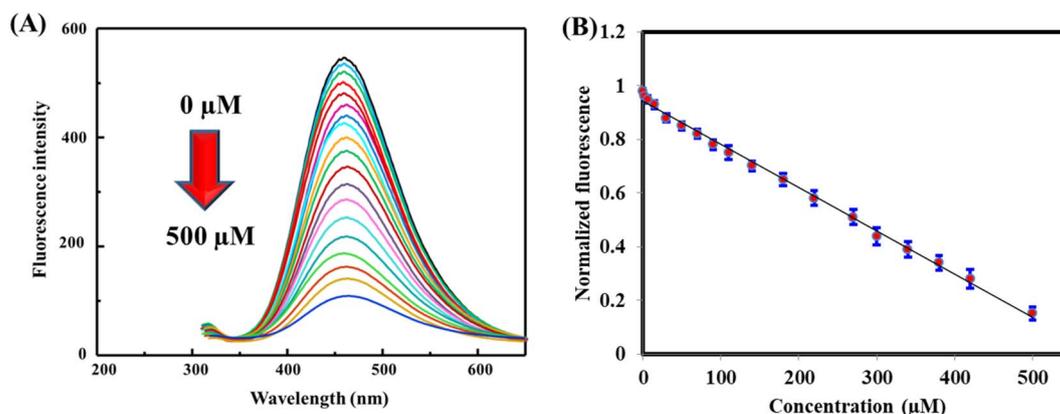

Fig. 4 (A) Fluorescence responses of biowaste-derived NCDs (2 mg mL^{-1}) upon addition of different amounts of ISQ (0–500 μM) while (B) is calibration plot. Each data point represents the mean ± SD of three independent measurements (*n* = 3).

Table 1 Comparative analysis of key analytical parameters for ISQ detection using the proposed NCDs-based method and previously reported techniques

Technique	Linear range (μM)	LOD (μM)	Per-sample cost ($)	Material input	Synthesis time	Reference
Capillary electrophoresis	1–500	0.29	~1.20	Buffer + capillary + voltage source	10 min per run	6
HPLC	0.01–0.08	0.0018	~1.50–2.00	Organic solvents (H_2O/ACN), columns	60 min per run	7
Fluorescence	0–50	0.056	~1.50–2.50	Lemon peels + melamine	6 hours	54
	0–500	0.0029	~0.04	Potato peels	4 hours	This work

material processing. Future work should explore continuous-flow synthesis strategies, cytotoxicity profiling, and detailed environmental life-cycle assessments to support industrial translation and regulatory compliance.

While the developed NCD-based probe demonstrated superior performance over conventional CE and HPLC methods in terms of detection speed, simplicity, and environmental footprint, its novelty is further reinforced when benchmarked against existing fluorescent carbon dot sensors derived from other biomass sources. As summarized in Table 2, the current system exhibits one of the lowest LODs (2.9 nM) and highest quantum yields (44.76%) among biomass-derived CDs reported for analyte detection. Compared to carbon dots synthesized from Rambutan seeds, black pepper, or chicken feet, the potato peel-based NCDs not only deliver enhanced sensitivity but also demonstrate exceptional stability under thermal, photonic, ionic, and pH fluctuations, broadening their application scope. The use of nitrogen doping capitalizes on the inherent amino-rich composition of potato peel, resulting in increased surface defects, improved charge distribution, and stronger interaction with analytes such as ISQ.[52,53] These combined attributes make the proposed platform a compelling, eco-friendly alternative for ultrasensitive detection, especially in resource-limited or field-deployable contexts.

3.5. Precision

Method precision was rigorously assessed at three representative ISQ concentrations (1.0, 50.0, and 200.0 μM) using five independently synthesized batches of NCDs under identical hydrothermal conditions. The intra- and inter-day relative standard deviations (RSDs) were consistently below 3.65% (Table 3), substantially lower than the acceptance threshold of 15% outlined by the ICH M10 bioanalytical method validation guidelines.[57,58] This high level of reproducibility underscores the robustness of the proposed assay and its reliability for routine implementation. Furthermore, the markedly low variability across both low and high concentration ranges highlights the method's potential for accurate monitoring in diverse analytical scenarios, including pharmacokinetic profiling and therapeutic drug monitoring, where long-term consistency and precision are critical.

3.6. Selectivity and anti-interference studies

The selectivity of the proposed sensing platform was systematically examined by monitoring its response toward 30 μM ISQ in the presence of a 10-fold molar excess of common potential interferents, including representative inorganic ions (Na^+, K^+, Ca^{2+}, Mg^{2+}, Cl^-, SO_4^{2-}, *etc.*) and biomolecules (such as glucose, ascorbic acid, and uric acid). As illustrated in Fig. 5, ISQ was the only analyte that produced a pronounced fluorescence quenching effect, whereas all other species elicited negligible changes in emission intensity. Moreover, co-incubation studies demonstrated that the interferents did not compromise or enhance the ISQ-mediated quenching signal, thereby confirming the exceptional specificity of the probe. This high selectivity is critical for real-sample applicability, ensuring reliable performance even in complex biological matrices where competing ions and biomolecules are abundant. The ability of

Table 2 Analytical figures of merit of the proposed NCDs and other NCDs in literature prepared from various biowastes

Carbon source	Heteroatom	Analyte	LOD (μM)	Linear range (μM)	Quantum yield (%)	Stability features	Reference
Potato peels	N	ISQ	0.0029	0–500	44.76	Thermo/photo/pH/ionic/storage conditions	This work
Black pepper	N	Ascorbic acid	0.3	0.5–50.0	10.25	Photo/pH/storage conditions	24
Rambutan seed biowaste	N	Congo red	0.035	0–10	16.87	Thermo/photo/ionic/storage conditions	28
Chicken feet	N	Diosmin	0.003	0.1–12	42.9	Thermo/photo/pH/ionic conditions	31
Coffee waste	B	Dopamine	0.004	0–30	17.5	Thermo/pH	53
Banana peels	N	Dopamine	0.168	0–300	35.37	Thermo/photo/pH/ionic/storage conditions	55
Sugarcane bagasse	N	Tetracycline	0.01	0–110	24.81	Not reported	56

Table 3 Precision of the biowaste-based NCDs for detecting ISQ

Concentration added (μM)	Matrix	Within day precision (n = 6)			Between days precision (n = 6)		
		Found (μM) ± SD	Recovery %	RSD %	Found (μM)) ± SD	Recovery %	RSD %
1.0	Phosphate buffer	0.98 ± 0.07	98.0	2.45	1.04 ± 0.08	104.0	3.46
50.0	(0.1 M, pH 7.0)	51.87 ± 0.18	103.7	2.06	51.97 ± 0.25	103.9	2.76
200.0		196.78 ± 0.20	98.4	3.10	203.43 ± 0.27	101.7	3.65

the sensor to maintain discriminative recognition under such challenging conditions highlights its promise for clinical diagnostics and pharmacological monitoring.

3.7. Applications

The practical applicability of the biomass-derived NCD probe was further established through quantitative analysis of ISQ in both pharmaceutical formulations and human serum samples.

Fig. 5 Fluorescence responses (A) and corresponding bar chart (B) of the biowaste-dependent NCDs probe in the absence (selectivity) and presence (anti-interference) of 30 μM ISQ with a 10-fold excess of interfering species, including inorganic ions and biomolecules as follows: 1. ISQ, 2. Na^+, 3. K^+, 4. Ca^{2+}, 5. Zn^{2+}, 6. Ba^{2+}, 7. Cl-, 8. SO_4^{2-}, 9. PO_4^{3-}, 10. Uric acid, 11. Dopamine, 12. Glucose, 13. Glutathione 14. Glycine, 15. Cholesterol, 16. Cysteine, 17. Lysine, 18. Alanine, 19. Phenylalanine, 20. Histidine, 21. Glutamic acid, 22. Tryptophan, 23. Ascorbic acid.

The method achieved recovery values ranging from 96.3% to 105.0%, with relative standard deviations not exceeding 3.78% (Table 4), underscoring excellent accuracy, reproducibility, and compliance with ICH M10 bioanalytical validation criteria. Importantly, no statistically significant differences were observed when benchmarked against an established reference method,[6] confirming the robustness and reliability of the developed sensor. Beyond demonstrating analytical performance, these findings highlight the probe's potential as a cost-effective and environmentally sustainable alternative to conventional detection systems. The combination of wide linearity, high sensitivity, and operational simplicity positions biomass-based NCDs as a promising platform for therapeutic drug monitoring, pharmacokinetic profiling, and routine quality control in pharmaceutical and clinical settings. Compared with previously reported fluorescent nanomaterials, the present system offers advantages in terms of green synthesis, reduced cost, and improved compatibility with complex biological matrices, reinforcing its translational potential.

While the NCD-based sensor demonstrated excellent recovery and precision in spiked serum and pharmaceutical tablet matrices, further validation in authentic clinical or environmental samples is necessary to fully establish its practical applicability. Real biological fluids such as whole plasma, urine, or tissue lysates contain a diverse array of high-abundance proteins (e.g., albumin, globulins), lipids, and other macromolecules that can adsorb onto nanoparticle surfaces, potentially altering fluorescence properties through nonspecific binding, shielding, or aggregation. These interactions may influence quenching dynamics, limit accessibility of the analyte to surface-active sites, or generate background fluorescence. Although sample pre-treatment (e.g., protein precipitation, centrifugation, buffer dilution) was used to minimize matrix effects, such steps may not fully replicate the complexity encountered in clinical diagnostics, where interfering species coexist in high concentrations. Compared to antibody-based assays or chromatographic techniques like HPLC, which incorporate rigorous sample cleanup and intrinsic molecular specificity, the current fluorescence-based approach offers speed and simplicity but may be more susceptible to nonspecific interactions. Therefore, future work should include validation in untreated or minimally processed clinical samples (e.g., patient serum, urine, or tissue extracts), coupled with interference profiling from endogenous macromolecules. This would enhance confidence in the method's robustness under
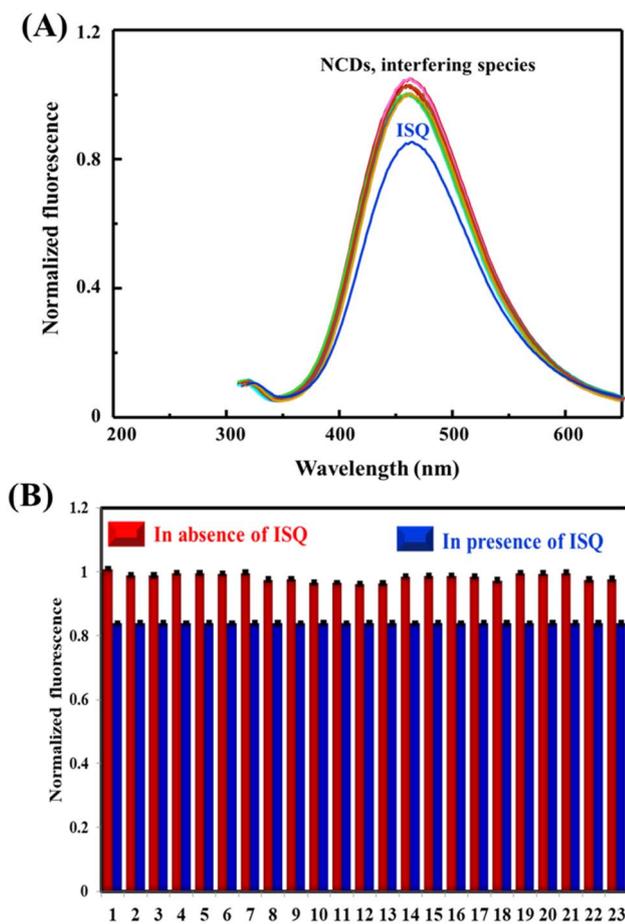
Table 4 Quantitative determination of ISQ in real samples using biomass-based probe ($n = 3$)

Matrix	Added (μM)	Biomass-derived CDs			CE[6]		
		Found (μM)	Recovery %	RSD %	Found (μM)	Recovery %	RSD %
Tablets	0.0	24.67 ± 0.27	—	—	24.45 ± 0.32	—	—
	1.0	25.68 ± 0.18	101.0	3.16	25.48 ± 0.27	103.0	3.56
	2.0	26.77 ± 0.20	105.0	3.05	26.34 ± 0.22	94.5	2.89
	3.0	27.56 ± 0.14	96.3	2.56	27.56 ± 0.30	103.7	3.99
Human serum	0.0	—	—	—	—	—	—
	1.0	0.98 ± 0.11	98.0	2.85	1.05 ± 0.24	105.0	4.23
	5.0	4.87 ± 0.23	97.4	3.78	5.13 ± 0.28	102.6	3.96
	10.0	9.87 ± 0.12	98.7	3.32	9.65 ± 0.21	96.5	4.09

physiological conditions and better define its comparative advantages or limitations relative to established analytical platforms.

4. Conclusion

This study presents a sustainable strategy for synthesizing NCDs from potato peel biowaste, yielding a low-cost and highly fluorescent probe for sensitive detection of ISQ. The NCDs demonstrated high quantum yield, stability across physico-chemical conditions, and strong analytical performance in model pharmaceutical and biological matrices. However, despite these promising results, the transition to routine clinical, environmental, or point-of-care use remains contingent upon overcoming key limitations. These include: (i) ensuring colloidal stability and shelf-life under physiologically relevant conditions, (ii) conducting *in vitro* and *in vivo* toxicity studies to confirm biocompatibility, (iii) understanding the fate, metabolism, and clearance of the NCDs in biological systems, and (iv) addressing potential nonspecific interactions or adsorption in protein-rich fluids. Additionally, scaling up synthesis while maintaining batch consistency and purity poses challenges that must be resolved for regulatory approval and industrial application. Future work should focus on integrating NCDs into standardized sensing platforms, assessing long-term environmental impact, and aligning fabrication processes with good manufacturing practices. In this context, the present study serves as a compelling proof-of-concept—highlighting both the potential and the critical translational hurdles of green nanomaterials in biomedical sensing.

Conflicts of interest

The authors declare no competing interests.

Data availability

Data will be available upon request from the corresponding authors.

Supplementary information (SI) is available. See DOI: **https://doi.org/10.1039/d5ra07665j**.

Acknowledgements

References

1 T. Yokoyama, K. Hisatomi, S. Oshima, I. Tanaka, T. Okada and N. Toyookam, *Eur. J. Med. Chem.*, 2024, **279**, 116836.

2 J. J. Li, J. Gu, S. J. Pan, N. Deng, M. Khan, L. Y. Li, X. Wu and Y. M. Li, *Cell. Signal.*, 2025, **131**, 111752.

3 H. Husseini Atteia, E. Saad Alamri, N. Sirag, N. Salah Zidan, R. Humod Aljohani, S. Alzahrani, M. Hamed Arafa, N. Sameeh Mohammad, M. Elsayed Asker, S. A. Zaitone and A. Tawfik Sakr, *Life Sci.*, 2023, **317**, 121460.

4 Y. H. Huang, J. Sun, S. L. Li, Y. F. Shi, L. G. Yu, A. M. Wu and X. Y. Wang, *Free Radical Biol. Med.*, 2024, **225**, 98–111.

5 S. Wei, L. Deng, S. L. Chen, X. Hu and G. W. Zhang, *Food Biosci.*, 2024, **59**, 104227.

6 Y. H. Cao, Y. Wang, C. Ji and J. N. Ye, *J. Chromatogr., A*, 2004, **1042**, 203–209.

7 J. B. Xie, W. Q. Wang, Y. Q. Zhang, Y. Bai and Q. Yang, *J. Pharmaceut. Biomed.*, 2007, **45**, 450–455.

8 A. M. Mahmoud, M. M. El-Wekil, R. Ali, H. A Batakoushy and R. Y. Shahin, *Microchim. Acta*, 2022, **189**, 183.

9 A. M. Mahmoud, M. H. Mahnashi, F. M. Alshareef and M. M. El-Wekil, *Microchem. J.*, 2023, **187**, 108430.

10 R. M. K. Mohamed, S. H. Mohamed, A. M. Asran, I. H. Alsohaimi, H. M. A. Hassan, H. Ibrahim and M. M. El-Wekil, *Spectrochim. Acta, Part A*, 2023, **293**, 122444.

11 A. M. Mahmoud, M. H. Mahnashi and M. M. El-Wekil, *Spectrochim. Acta, Part A*, 2024, **304**, 123347.

12 B. A. Alyami, A. M. Mahmoud, A. O. Alqarni, A. B. H. Ali and M. M. El-Wekil, *Microchim. Acta*, 2023, **190**, 467.

13 R. Naidu, B. Biswas, I. R. Willett, J. Cribb, B. K. Singh, C. P. Nathanail, F. Coulon, K. T. Semple, K. C. Jones, A. Barclay and R. J. Aitken, *Environ. Int.*, 2021, **156**, 106616.

14 M. A. Yahya, Z. Al-Qodah and C. W. Z. Ngah, *Sustain. Energy Rev.*, 2015, **46**, 218–235.

15 S. Kaur and L. Sarao, Bioenergy from agricultural wastes. *Bioenergy Research: Biomass Waste to Energy*, Springer, 2021, pp. 127–147.

16 C. Cheng, Y. Shi, M. Li, M. Xing and Q. Wu, *Mater. Sci. Eng., C*, 2017, **79**, 473–480.

17 S. Perumal, R. Atchudan, T. N. J. I. Edison and Y. R. Lee, *J. Environ. Chem. Eng.*, 2021, **9**, 105802.

18 P. Zong, Y. Jiang, Y. Tian, J. Li, M. Yuan, Y. Ji, M. Chen, D. Li and Y. Qiao, *Energy Convers. Manage.*, 2020, **216**, 112777.

19 Z. Liu and R. Balasubramanian, *Appl. Energy*, 2014, **114**, 857–864.

20 R. Atchudan, T. N. J. I. Edison and Y. R. Lee, *J. Colloid Interface Sci.*, 2016, **482**, 8–18.

21 A. Z. Alanazi, K. Alhazzani, A. M. Mostafa, J. Barker, M. M. El-Wekil and A. M. B. H. Ali, *Microchem. J.*, 2024, **197**, 109800.

22 A. M. Mahmoud, M. H. Mahnashi, S. A. Alkahtani and M. M. El-Wekil, *Int. J. Biol. Macromol.*, 2020, **165**, 2030–2037.

23 A. O. Alqarni, S. A. Alkahtani, A. M. Mahmoud and M. M. El-Wekil, *Spectrochim. Acta, Part A*, 2021, **248**, 119180.

24 C. Tang, R. Q. Long, X. Tong, Y. Guo, C. Y. Tong and S. Y. Shi, *Microchem. J.*, 2021, **164**, 106000.

25 Z. R. Yin, H. W. Wang, X. D. Tang, M. S. Mou, H. M. Yu and H. Y. Wang, *Spectrochim. Acta, Part A*, 2025, **330**, 125746.

26 M. H. Mahnashi, A. M. Mahmoud, M. M. El-Wekil and R. Y. Shahin, *Microchem. J.*, 2023, **193**, 109062.

27 M. N. Goda, L. S. Alqarnia, H. Ibrahim, A. B. H. Ali and M. M. El-Wekil, *RSC Adv.*, 2025, **15**, 28375–28383.

28 M. Zulfajri, S. Sudewi, R. Damayanti and G. G. Huang, *RSC Adv.*, 2023, **13**, 6422–6432.

29 Y. A. Bin Jardan, A. M. Mostafa, J. Barker, A. B. H. Ali and M. M. El-Wekil, *Anal. Methods*, 2025, **17**, 3007–3016.

30 A. M. Mahmoud, M. H. Mahnashi, A. Al Fatease, M. A. H. Mostafa, M. M. El-Wekil and R. Ali, *J. Food Compos. Anal.*, 2022, **108**, 104428.

31 A. M. Mahmoud, S. S. Abu-Alrub, A. O. Alqarni, M. M. El-Wekil and A. B. H. Ali, *Microchem. J.*, 2023, **191**, 108929.

32 A. Z. Alanazi, K. Alhazzani, H. Ibrahim, A. B. H Ali, M. Darweesh, R. Y Shahin and M. M. El-Wekil, *Microchem. J.*, 2024, **206**, 111625.

33 S. T. Alsharif, A. M. Mahmoud, M. M. El-Wekil and A. B. H. Ali, *Microchem. J.*, 2025, **208**, 112618.

34 M. Yang, Y. Yan, E. Liu, X. Hu, H. Hao and J. Fan, *Opt. Mater.*, 2021, **112**, 110743.

35 M. E. El Sharkasy, M. M. Tolba, F. Belal, M. I. Walash and R. Aboshabana, *Spectrochim. Acta, Part A*, 2023, **289**, 122246.

36 A. B. H. Ali, M. R. Elmasry, Y. A. Bin Jardan and M. M. El-Wekil, *J. Photochem. Photobiol., A*, 2025, **466**, 116416.

37 A. B. H. Ali, A. Mostafa, J. Barker, Y. A. Bin Jardan and M. M. El-Wekil, *Microchem. J.*, 2025, **213**, 113704.

38 L. Wang, Y. Bi, J. Gao, Y. Li, H. Ding and L. Ding, *RSC Adv.*, 2016, **6**, 85820–85828.

39 L. N. Wu, H. P. Xiao, J. X. Xue, X. Y. Lin, Z. M. Zhu, A. L. Liu and L. Q. Lin, *Anal. Chim. Acta*, 2025, **1355**, 343983.

40 Y. X. Chen, C. Wang, Y. S. Guo, W. X. Yang, G. L. Zhang and Q. H. Wu, *Microchem. J.*, 2025, **209**, 112750.

41 G. Alasiri, A. M. Alaseem, A. B. H. Ali, R. Ali and M. M. El-Wekil, *Microchem. J.*, 2025, **218**, 115156.

42 A. M. Alaseem, G. Alasiri, M. M. El-Wekil and A. B. H. Ali, *Microchem. J.*, 2025, **218**, 115361.

43 A. M. N. Goda, L. S. Alqarni, H. Ibrahim, M. M. El-Wekil and A. B. H. Ali, *J. Photochem. Photobiol., A*, 2025, **468**, 116535.

44 B. S. Kadian and G. Manik, *Food Chem.*, 2020, **317**, 126457.

45 C. J. Wang, R. Sheng Li, H. Zhi Zhang, N. Wang, Z. Zhang and C. Z. Huang, *Biosens. Bioelectron.*, 2017, **97**, 157–163.

46 D. Y. Ren and Z. Fan, *Food Chem.*, 2023, **416**, 135792.

47 E. P. K. Behera and A. K. Mishra, *J. Photochem. Photobiol., A*, 1993, **71**, 115–118.

48 F. M. Shaw, D. Samanta, A. S. Shaik, A. Bhattacharya, R. Basu, I. Mondal and A. Pathak, *Opt. Mater.*, 2023, **137**, 113600.

49 G. Y. Guo, Z. Huang, L. Wang, X. Gao, Y. Chen, F. Lu, C. Sun, H. Li, H. Li, Y. He, W. Yan, L. Liu and J. Qu, *Anal. Chem.*, 2025, **97**, 5744–5752.

50 R. A. Emam, G. Magdy, F. Belal and A. A. Emam, *Microchem. J.*, 2025, **212**, 113248.

51 H. V. M. Naik, S. V. Bhosale and G. B. Kolekar, *Anal. Methods*, 2022, **14**, 877–891.

52 R. Ali, H. Elfadil, N. Sirag, A. S. Albalawi, A. Albalawi, S. Alharbi, A. Al-anzi, S. Alatawi, Y. Alhuaiti, F. T. Alsubaie, N. Aldwsari and M. M. El-Wekil, *Microchem. J.*, 2025, **212**, 113376.

53 R. Sangubotla, S. Won and J. Kim, *J. Photochem. Photobiol., A*, 2023, **438**, 114542.

54 Y. Zhang, Z. Zhao and H. Wu, *Spectrochim. Acta, Part A*, 2025, **343**, 126554.

55 L. Han, Y. Guo, H. Zhang, Z. Wang, F. Zhang, Y. Wang, X. Li, Y. Wang and J. Ye, *RSC Adv.*, 2024, **14**, 1813–1821.

56 A. A. Alfi, N. A. Alamrani, O. A. Azher, R. M. Snari, H. M. Abumelha, Z. A. Al-Ahmed and N. M. El-Metwaly, *J. Mater. Res. Technol.*, 2022, **19**, 4697–470.

57 P. Y. Khashaba, H. R. H. Ali and M. M. El-Wekil, *Spectrochim. Acta, Part A*, 2018, **190**, 10–14.

58 M. M. El-Wekil, K. K. Abdelhady, R. A. Abdel Salam and G. M. Hadad, *Spectrochim. Acta, Part A*, 2019, **213**, 249–253.